Zinc-Induced Liquid Metal Embrittlement in Austenitic Microstructures

This study explores the impact of liquid metal embrittlement cracking on the tensile properties and failure mechanism of an austenitic microstructure

BY A. GHATEI-KALASHAMI AND Y. N. ZHOU

Abstract

The problem of liquid metal embrittlement (LME) is one of the main concerns to be addressed when developing high-strength automotive steels. Although LME has been extensively investigated over the past decade, the role of LME-induced cracking on the failure mechanism of steel substrates has not been adequately explored. This study investigates the influence of LME cracking on the tensile properties and failure mechanism of an austenitic microstructure. An in-depth analysis of the LME crack propagation path revealed that the crack propagated predominantly along high-angle, random grain boundaries. The detailed failure analysis showed that the Zn-coated austenitic steel failed in an intergranular mechanism without any plastic strain being applied to the grains during deformation. The results of the study indicate that stress-assisted grain boundary diffusion is responsible for the premature failure of Zn-coated austenitic microstructures at much lower tensile stresses than that of the uncoated specimen. It was found that the application of thermomechanical conditions characterized by low stress and low temperature, combined with microstructures featuring a low Zn grain boundary diffusion rate, can effectively reduce LME cracking.

Keywords

- Liquid Metal Embrittlement (LME)
- Crack Propagation
- Failure Mechanism
- Advanced High Strength Steels (AHSS)

https://doi.org/10.29391/2024.103.029

Introduction

Advanced high-strength steels (AHSS) offer an exceptional combination of high/ultrahigh strength and remarkable ductility, making them an excellent material for reducing vehicle weight while maintaining passenger safety (Ref. 1) However, AHSS are susceptible to corrosion; therefore, zinc (Zn) coatings are commonly applied to protect them from corrosive environments (Refs. 4, 5). The Zn coating protects the steel in two distinct ways (Ref. 6): first, it provides barrier protection by physically separating steel from the corrosive environment. Second, Zn is used as a galvanic anode where it corrodes in place of steel when exposed to corrosive media (Ref. 6). Although a Zn coating offers protection from corrosion, it may result in liquid metal embrittlement (LME) cracking during subsequent manufacturing steps, such as hot stamping (Refs. 7, 8) and resistance spot welding (RSW) processes (Refs. 2, 9, 11).

LME is an intergranular degradation phenomenon that occurs when a ductile metal (e.g., AHSS) is exposed to liquid metal (e.g., liquid Zn) while simultaneously experiencing a tensile load (Ref. 12). The LME in Zn-coated steels (hereafter called the Fe-Zn system) exhibits some distinctive characteristics that distinguish it from other LME couples (Ref. 13). For instance, the LME cracking in the Fe-Zn system most commonly occurs at a high temperature (i.e., higher than 650°C [1202°F]) (Refs. 14–15), which is beyond the critical temperature for ferrite to austenite transformation in most families of AHSS (Ref. 16). Due to this nonequilibrium phase transformation, the effect of metallurgical factors, such as initial microstructural or grain boundary characteristics, on LME crack susceptibility remains unclear. For example, it is frequently reported that austenitic microstructures have the highest susceptibility to LME cracking, whereas ferritic microstructures exhibit low LME susceptibility (Refs. 12, 17). This led to the conclusion that a fully ferritic decarburization layer could be used as a technique for mitigating LME cracks in AHSS (Ref. 18). This strategy has the potential to be effective in certain thermomechanical conditions (Ref. 12); however, recent investigations have shown that LME

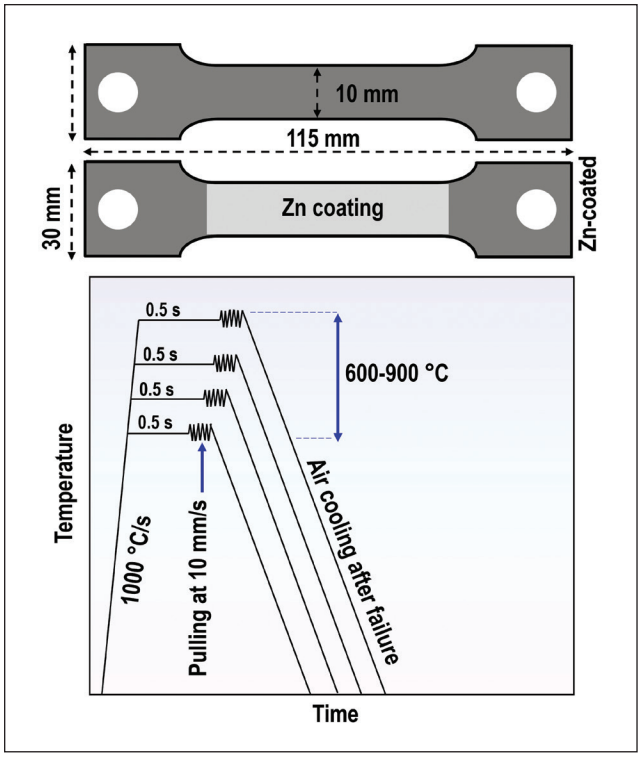

Fig. 1 — Schematic illustration of the uncoated and Zn-coated tensile test specimens along with the thermomechanical process parameters used in this study to investigate LME cracking in austenitic steel.

cracking occurs in a fully ferritic decarbonization layer in dual-phase (DP) (Ref. 19) and quenched and partitioned (Q&P) steels (Refs. 20–21). Additionally, LME cracks were observed in the subcritical heat-affected zone (SCHAZ) during RSW of transformation-induced plasticity (TRIP) steel, further indicating that LME cracking can occur in ferric-martensitic microstructures (Ref. 22).

To resolve the controversy regarding the role of metallurgical factors in LME crack susceptibility, extensive studies have been conducted on LME cracking in single-phase ferritic and austenitic microstructures (Refs. 12, 16, 17). While such microstructures may have a completely different chemical composition (e.g., high content of Ni and Cr) than AHSS (Refs. 12, 17), the knowledge gained from studying LME in such simple microstructures is perfectly applicable to AHSS. In recent studies by the present authors (Refs. 12, 17), LME crack susceptibility was examined in ferritic and austenitic microstructures, and it was found that both initial microstructures are susceptible to LME cracking. The ferritic microstructures were more prone to LME crack initiation with a low crack propagation rate, which resulted in a much higher frequency of smaller cracks. The austenitic microstructures were found to be resistant to crack initiation, while the LME crack propagation rate was significantly higher, resulting in fewer cracks that were much larger. Consequently, the results obtained in these studies were correlated with the target problem, which was the occurrence of LME cracks in fully ferric decarburization layers. It was found that due to the low LME crack propagation rate in ferritic microstructures, a decarburization layer may be an effective method for mitigating LME. However, under severe thermomechanical conditions during RSW and due to steel's chemical composition (e.g., Si content), numerous LME cracks can propagate rapidly, resulting in a higher LME susceptibility in a sample with a deeper decarburized layer (Refs. 12, 19).

The purpose of this study is to gain a better understanding of LME-induced cracking in the Fe-Zn system. Specifically, this study examines the effect of grain boundary misorientation and grain boundary character distribution on LME crack susceptibility. Additionally, the present study investigates the effects of LME-induced cracking on the failure behavior of austenitic structures, which facilitates a better understanding of the mechanisms responsible for LME crack propagation. The results of this study will contribute to a better understanding of this complex phenomenon in Zn-coated steels.

Materials and Methods

The as-received material was 304-type austenitic with a thickness of 1.0 ± 0.1 mm (0.039 ± 0.004 in.). The chemical composition of the steel per ASTM A240 (Ref. 23) is shown in Table 1. The Zn coating was applied to the steel panels using an electro-galvanizing (EG) process. The Zn coating layer thickness was approximately 10 µm.

The uncoated and Zn-coated specimens were subjected to the thermomechanical cycle of the high-temperature tensile test using a Gleeble 3500 thermomechanical simulator machine. The tensile specimens were cut into dog bone shapes using a ProtoMax waterjet cutter. The dimensions of the tensile test specimen, as well as the thermomechanical parameters used in this study, are shown in Fig. 1. A detailed description of the high-temperature tensile test can be found in Refs. 12 and 24. To determine LME severity, the tensile curves of Zn-coated samples were compared to the uncoated samples. The LME crack severity was quantified by calculating the ductility loss based on Equation 1:

$$\text{Ductility loss} = \frac{\text{Strain}_{(\text{bare})} - \text{Strain}_{(\text{coated})}}{\text{Strain}_{(\text{bare})}} \quad (1)$$

The fracture toughness of the uncoated and zinc-coated specimens was also assessed by measuring the area under stress-strain curves. Microstructural characterization was conducted by scanning electron microscope (SEM, JSM7001F), energy-dispersive spectroscopy (EDS), and electron backscatter diffraction (EBSD) methods. The EBSD samples were prepared with a conventional sample preparation procedure and a final vibratory polishing step. The postprocessing analysis of EBSD data was performed using the MTEX (Ref. 25) toolkit in MATLAB.

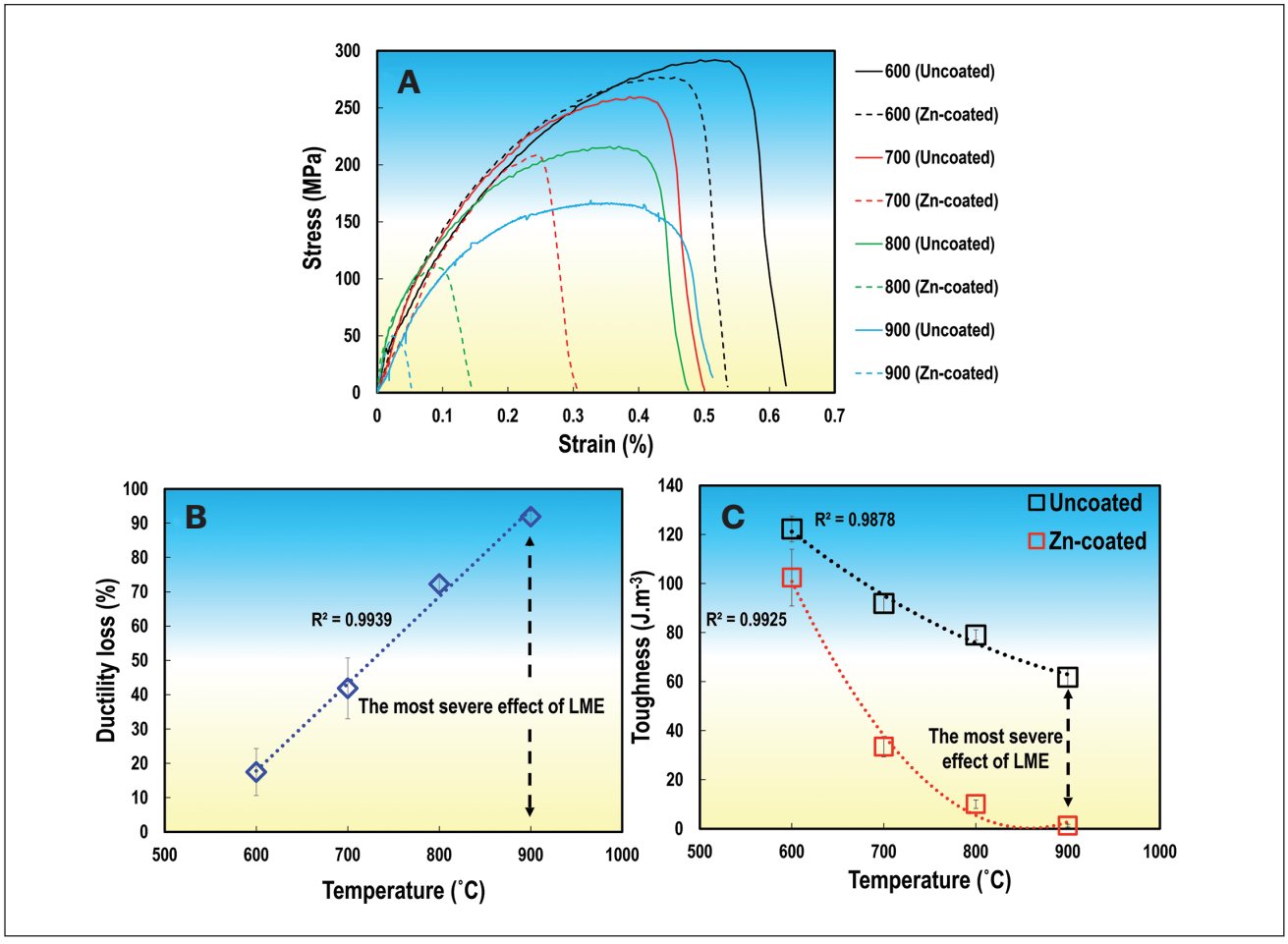

Fig. 2 — A — The strain-stress curves of the uncoated and Zn-coated specimens after high-temperature tensile testing at temperatures between 600 and 900°C; B — the variation of ductility loss as a function of testing temperature; C — the variation in the toughness of the uncoated and Zn-coated specimens at different tensile test temperatures.

Results

High-Temperature Tensile Properties

Figure 2A shows the representative strain-stress curves for uncoated and zinc-coated austenitic steels after tensile testing at temperatures between 600 and 900°C (1112 and 1652°F). The results indicate that there is a notable difference in tensile properties between the uncoated and Zn-coated specimens under the same thermomechanical conditions. Figure 2B illustrates the change in ductility between the Zn-coated specimen and the uncoated sample. Based on the results of the test performed at 600°C, the presence of the Zn coating led to a 20% reduction in the ductility of the austenitic steel substrate. Moreover, ductility loss increased significantly with the increasing testing temperature where approximately 90% of the steel substrate's ductility was lost after tensile testing at 900°C. This indicated that the deformation behavior of austenitic steel changed from a ductile behavior to a completely catastrophic brittle one. The variation of the fracture toughness of the specimens as a function of testing temperature is shown in Fig. 2C. With increasing testing temperature, the fracture toughness decreased, with the temperature of 900°C showing the greatest reduction in toughness in comparison to other testing temperatures. According to Fig. 2, the Zn-coated steel exhibited significantly lower tensile properties in terms of ductility and fracture toughness than uncoated steel. The primary reason for the transition from ductile to brittle behavior in the presence of Zn coating is associated with the formation of LME cracking in the Zn-coated samples. The results show that LME significantly affected the tensile properties of the austenitic microstructure at 900°C, with a 90% reduction in ductility and near zero toughness. Consequently, the uncoated and Zn-coated specimens after the tensile test at 900°C were characterized in detail to determine how LME-induced cracking can result in this substantial reduction of tensile properties.

Figure 3A illustrates the cross-sectional SEM micrograph of uncoated and Zn-coated specimens after the tensile test at 900°C. The uncoated sample failed in a ductile manner, exhibiting clear evidence of plastic deformation (i.e., necking) and voids at the fracture surface. The Zn-coated specimen, however, demonstrated an entirely brittle failure behavior

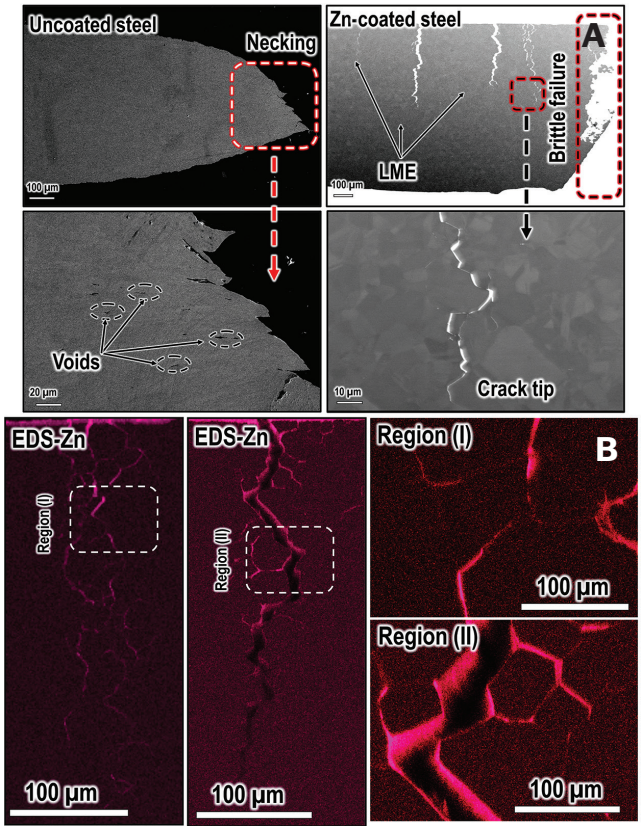

Fig. 3 — A — SEM micrographs of the cross sections of the uncoated and Zn-coated austenitic specimens after high-temperature tensile testing at 900°C; B — the EDS-Zn maps of the LME cracks formed in the Zn-coated specimen. The high-magnification EDS analysis was conducted in Region (I) and Region (II).

Table 1 — Chemical Nominal Composition (wt-%) of the As-Received Austenitic Steel

C	Mn	Si	Ni	Cr	Fe
0.08	2.00	0.75	8-12	18-20	Bal.

with no sign of plastic deformation (i.e., an almost flat fracture surface). Additionally, the SEM micrographs of the Zn-coated specimen showed several LME cracks that were formed in the area near the fracture surface. The results indicate that LME-induced cracking was the primary mechanism responsible for the degradation of the mechanical properties of the Zn-coated specimen. Figure 3B shows the EDS element maps of the LME cracks formed in the Zn-coated specimen. Results indicated the presence of Zn within the crack, which is one of the most prominent characteristics of a Zn-induced LME cracking. The high-magnification EDS analysis of the LME crack is also shown in Fig. 3 as indicated by Regions (I) and (II) in the EDS maps. The EDS maps show that Zn was penetrated along the grain boundary network of the steel substrate. The results confirm that the Zn melted and rapidly penetrated through the microstructure of the coated steel specimen, resulting in a significant reduction in the mechanical properties.

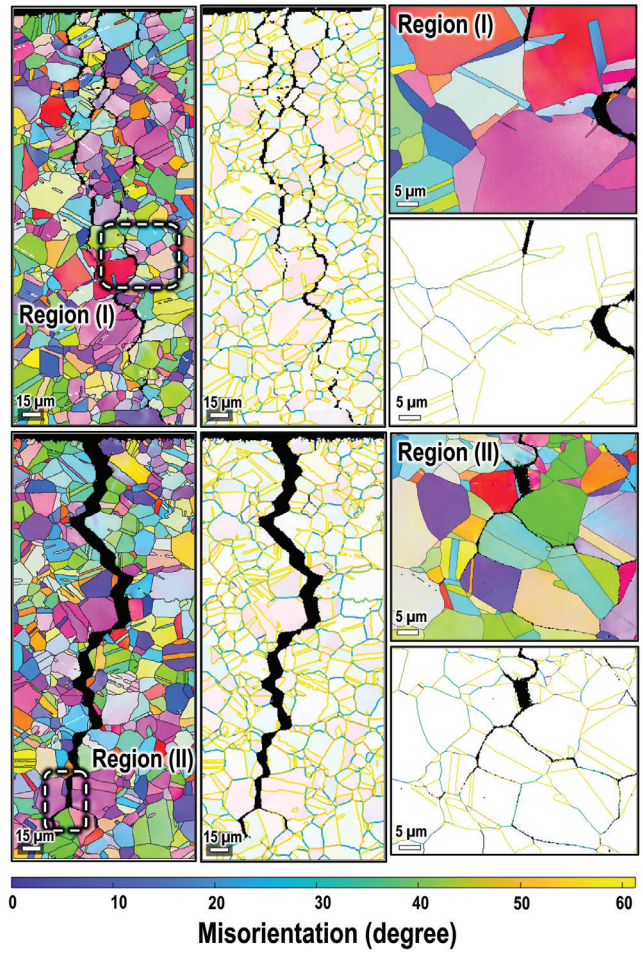

Fig. 4 — The EBSD-IPF maps along with grain boundary misorientation distribution in the vicinity of the LME cracks. The high-magnification EBSD analyses in two regions of the LME cracks are indicated as Region (I) and Region (II) in this figure.

LME Crack Characterization

To gain a deeper understanding of the role of LME cracking in the degradation of the mechanical properties of the austenitic steel substrate, the LME cracks were further characterized by EBSD analysis. Figure 4 shows the EBSD-IPF maps in the vicinity of the LME cracks of the austenitic specimen, which showed that the orientation of the grains on both sides of the LME cracks is different, indicating a crack propagated predominantly along the grain boundaries. This can be further confirmed by the high-resolution EBSD analysis of the LME crack (i.e., Regions [I] and [II] in Fig. 4), which indicated that LME cracks propagated along the grain boundaries. Moreover, the grain boundary misorientation distribution analysis showed that LME cracks only propagated along high-angle grain boundaries (i.e., misorientation higher than 15 deg), and no cracks were found along the low-angle boundaries (i.e., misorientation lower than 15 deg). The results are completely consistent with the literature (Ref. 26), further emphasizing the intergranular nature of LME cracking.

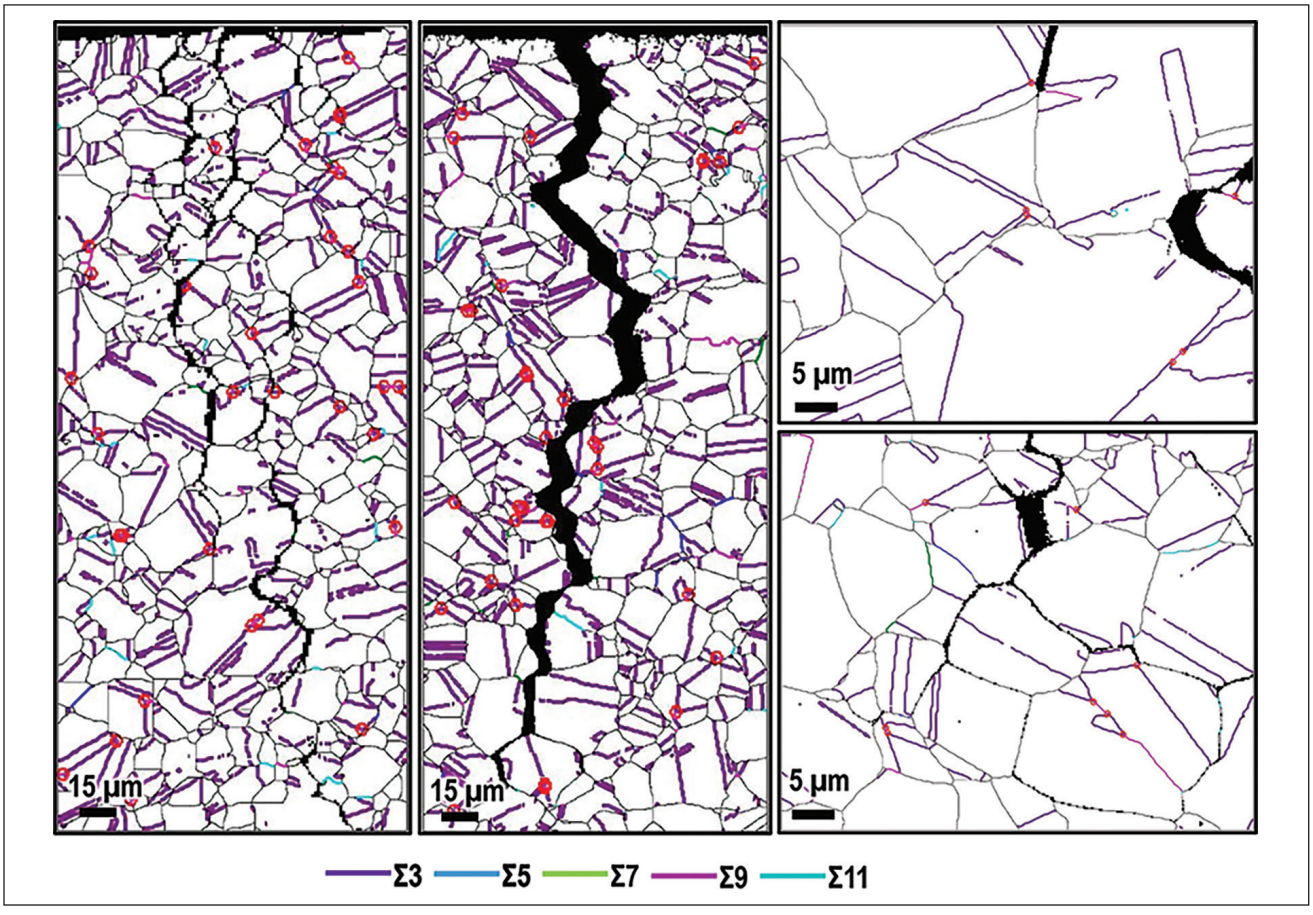

Fig. 5 — The distribution of coincidence site lattice (CSL) boundaries in the vicinity of the LME cracks, where black lines indicate random grain boundaries and colored lines represent CSL boundaries (i.e., Σ3, Σ5, Σ7, and Σ11). The red circles indicate triple junctions containing at least one CSL boundary.

As LME cracks propagated completely intergranular, the grain boundary characteristics of the steel substrate can have a significant impact on the crack propagation path. The analysis of grain boundary misorientation revealed that a high fraction of grain boundaries have a misorientation angle of 60 deg (i.e., yellow lines in Fig. 4). This specific misorientation angle between two grains corresponds to a coherent twin boundary (60 deg/<111>) that is consistently observed in steels with austenitic microstructures (Ref. 17) and TWIP steel (Ref. 27). It is evident from Fig. 4 that no LME cracks propagated along the twin boundaries. The twin boundaries have demonstrated to be highly resistant to various intergranular cracking phenomena such as stress corrosion cracking (Ref. 28), hydrogen embrittlement (Ref. 29), and LME cracking (Refs. 11, 30). This is due to the relatively ordered structure of the boundary and the low grain boundary energy of the boundary. Despite the existence of a high percentage of twin boundaries in the investigated austenitic steel, crack susceptibility to LME was higher in steel substrate than in ferritic steel with virtually no twin boundaries (Ref. 12).

Other than the grain boundary misorientation angle, the distribution of grain boundaries is also a key factor in determining the susceptibility of the steel to LME cracking. Consequently, the grain boundary character distribution (GBCD) maps were calculated to determine the significance

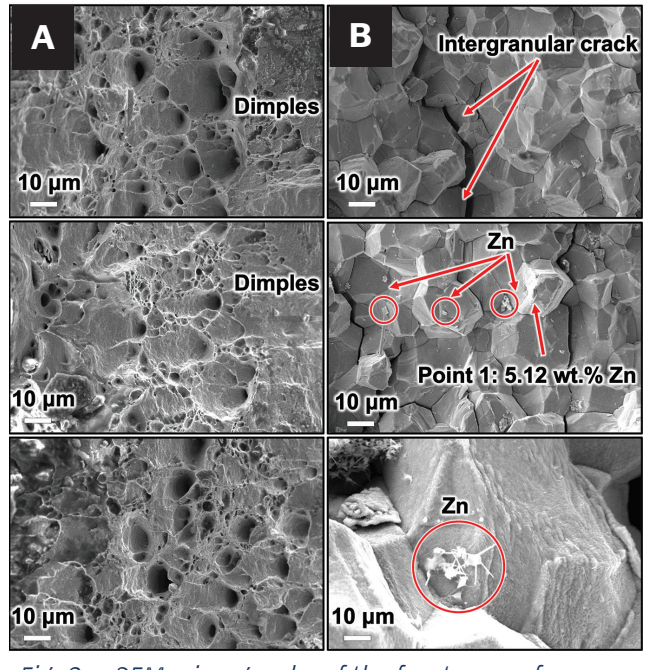

Fig. 6 — SEM micrographs of the fracture surface of the austenitic specimen after tensile testing at 900°C: A — uncoated specimen; B — Zn-coated specimen.

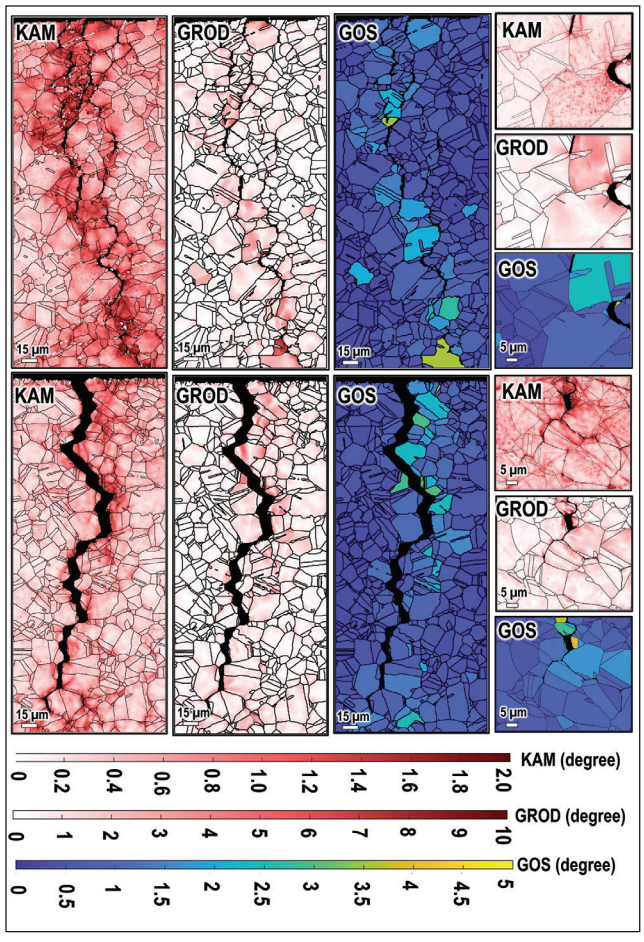

Fig. 7 — The plastic strain analysis in the vicinity of the LME cracks of the austenitic steel by kernel average misorientation (KAM), grain reference orientation deviation (GROD), and grain orientation spread (GOS) maps.

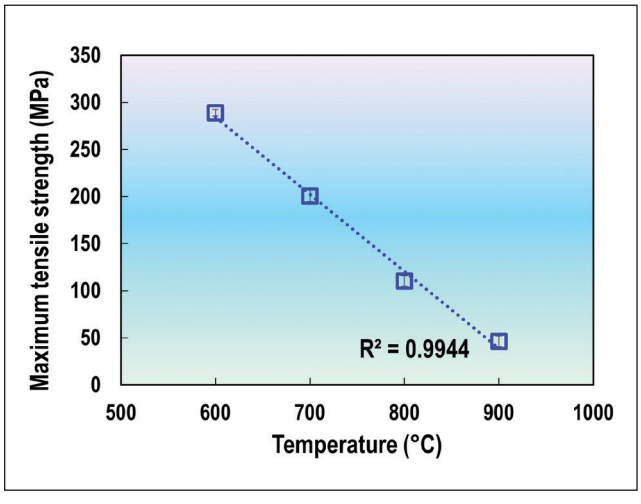

Fig. 8 — The variation of maximum tensile strength of the Zn-coated specimens as a function of test temperature.

of grain boundary type distribution in LME crack propagation behavior. In Fig. 5, black lines indicate random grain boundaries while colored lines represent coincidence site lattice (CSL) boundaries (i.e., Σ3, Σ5, Σ7, and Σ11). Additionally, the red circles in Fig. 5 are indicative of triple junctions containing at least one CSL boundary. Figure 5 clearly shows that LME cracks propagated only along random boundaries, while no cracks were observed propagating along twin boundaries (i.e., Σ3) or other low-index CSL boundaries. Furthermore, the LME cracks did not propagate along triple junctions containing at least one CSL boundary. The points are known to impede the propagation of cracks in numerous intergranular cracking phenomena (Refs. 30, 31). This implies that when the crack reached these junctions, it either completely stopped or changed direction, depending on the magnitude and direction of the applied tensile stress. Razmpoosh et al. (Ref. 26) investigated the effects of the grain boundary misorientation angle on the LME crack behavior during laser dissimilar welding of 304 stainless steel and Zn-coated Mn steel. The results showed that no LME cracking occurred in some specific misorientation angles such as ~38 deg and 60 deg that corresponded to Σ5 and Σ3 special boundaries, respectively (Ref. 26).

Failure Analysis

To investigate the effect of LME-induced cracking on failure behavior, fracture surfaces of the uncoated and Zn-coated austenitic microstructures were analyzed by fractography analysis. The SEM micrographs of the fracture surface of the uncoated specimen are shown in Fig. 6A. It is evident that a ductile fracture was the predominant mode of fracture for uncoated steel. It is known that ductile fractures occur in three stages (Ref. 32): (i) void nucleation, (ii) void growth, and (iii) void coalescence. Therefore, the uncoated sample failed in a completely ductile manner, in agreement with the results shown in Figs. 2 and 3. The SEM images of the fracture surface of the Zn-coated specimen are shown in Fig. 6B. The analysis of the fracture surface of the Zn-coated sample did not reveal any distinct indications of plastic deformation, such as voids, dimples, or slip lines. Conversely, the fracture surface of the Zn-coated sample presented intergranular cracks. Additionally, the EDS analysis confirmed the presence of liquid Zn on the fracture surface. The liquid Zn crystals observed at the fracture surface are consistent with the findings reported in the existing literature (Ref. 33). Murugan et al. (Ref. 33) studied Zn transport mechanisms in TRIP steel using fractography analysis and revealed a variety of Zn morphologies on the fracture surface, including a continuous film of Zn; discontinuous globules of Zn between two grains; and discontinuous, spike-like globules of Zn. The authors indicated that the liquid Zn penetrated the grain boundary and exhibited a considerable degree of wettability. It has been shown by the present authors in a recent study that austenitic microstructures exhibit an intergranular cracking morphology in contrast to ferritic microstructures, which exhibit a hybrid LME-induced failure pattern that exhibits both dimples and intergranular cracking (Ref. 12). This observation further confirms the high susceptibility of the austenitic microstructure to LME cracking. Furthermore, the

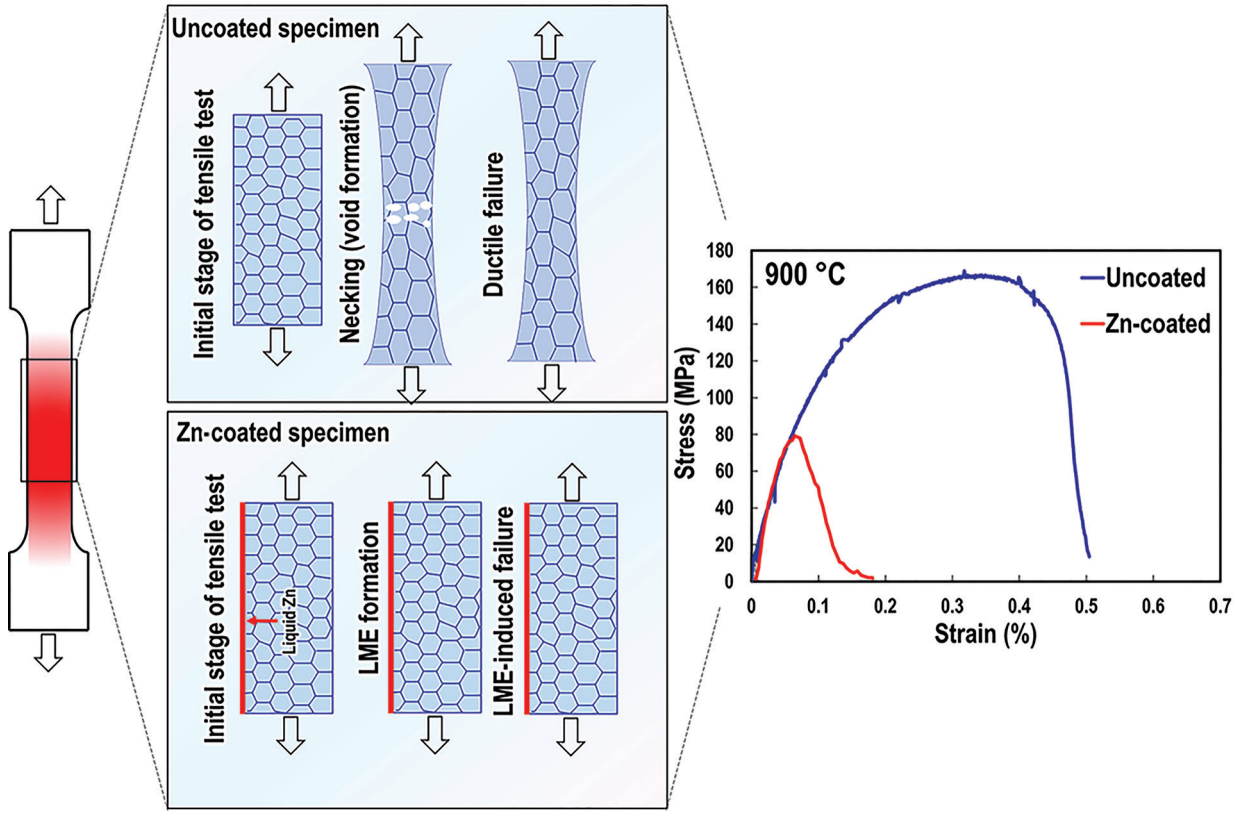

Fig. 9 — The schematic illustration of the role of LME-induced cracking in the failure mechanism of the austenitic steel during the high-temperature tensile test. (The stress-stain curve was adopted from the data presented in Fig. 1 for the testing temperature of 900°C to illustrate how Zn-induced LME cracking affected the tensile properties of the austenitic steel.)

lack of plastic deformation during LME crack propagation was evident in Fig. 6B, which clearly shows that the grains between the intergranular cracks were not affected during the high-temperature tensile test.

To further investigate whether LME crack propagation is associated with plastic deformation activity or has a brittle behavior, the plastic strains of the grains were calculated for both low-magnification and high-resolution EBSD data. Figure 7 shows the kernel average misorientation (KAM), grain reference orientation deviation (GROD), and grain orientation spread (GOS) maps in the vicinity of the LME cracks. KAM refers to the average misorientation between a kernel point and its neighbors, excluding those outside the grain boundary, which reflects the local lattice curvature and can be used to map the mesoscopic strain distribution of grains (Ref. 34). Based on the KAM maps of the investigated LME cracks, it is evident that the grains near the cracks experienced a high degree of plastic deformation, in contrast to grains located further away from the cracks that appear to have been unaffected by plastic deformation.

The GROD and GOS maps were also constructed from EBSD data to shed more light on the possibility of plastic deformation activity during LME crack propagation. A GROD map shows in-grain misorientations relative to the selected reference orientation, which provides a better estimate of plastic deformation than other misorientation parameters (such as KAM) as it does not depend on the step size of the EBSD data (Ref. 35). GOS refers to the deviation in orientation between each scan point contained within a grain and the grain's average orientation (Ref. 36). It can be seen from Fig. 7 that the grains did not experience any plastic deformation during crack propagation. However, only grains very close to LME cracks showed higher GROD and GOS values. The results indicate that the plastic strain was distributed inhomogeneously and was limited to the grains on both sides of the LME crack. The results agree with the fractography analysis, which shows that LME cracking occurred completely brittlely without any plastic deformation.

Discussions

The results presented in this study clearly show that austenitic steel has a high susceptibility to LME cracking at temperatures within the range of 600 to 900°C. It was also shown that the susceptibility of the investigated austenitic steel to LME cracking increased with the increasing testing temperature where, after the tensile test at 900°C, the sample showed a complete transition from ductile to brittle behavior. It is known that LME-induced cracking occurs rap-

idly during the high-temperature tensile test, resulting in a significant reduction in the ductility of the steel substrate (Refs. 12, 37, 38). Additionally, it is known that LME cracking occurs in the Zn-coated steels within a temperature range known as the "ductility trough" (Refs. 14, 38–42), which indicates that the most severe reduction in tensile properties occurs in this temperature range. The LME temperature range varied between 700° and 900°C for various types of steel substrates (Refs. 14, 38–42). The results presented in Fig. 2 show that LME cracking occurred at temperatures between 600° and 900°C, which indicates that the investigated austenitic steel is highly susceptible to the formation of LME cracks.

According to strain analysis by EBSD maps (Fig. 7), two important aspects of LME cracking were revealed. First, LME crack propagation occurred in a completely brittle manner, and the specimen did not undergo any plastic deformation during the cracking process. This is entirely consistent with the high-temperature tensile test results, which indicate that the Zn-coated specimen failed due to a brittle failure mechanism. Second, it was shown that tensile stress is an essential prerequisite for the occurrence of LME cracking, as only grains close to cracks showed high KAM values, indicating that tensile stress was present during crack propagation, but its magnitude was insufficient to cause plastic deformation.

The degradation in the tensile properties of the Zn-coated specimens can be explained by the mechanism responsible for the formation of LME cracks in the Fe-Zn couple. Recent investigations have revealed that the stress-assisted grain boundary diffusion mechanism (also known as the Gordon-An mode [Ref. 43]) is the most plausible explanation for the occurrence of LME cracks in different families of Zn-coated steels (Refs. 42, 44, 45). According to this mechanism, Zn atoms first diffuse along grain boundaries of steel due to an atomic diffusion mechanism, resulting in a decrease in grain boundary cohesion. The presence of tensile stress results in cracking along the susceptible grain boundary, allowing liquid Zn to flow into the crack area, leading to the formation of LME cracks (Refs. 17, 43). The role of Zn in the decohesion mechanisms of the steel grain boundary has been recently explored through density functional theory (DFT) calculations comparing the tensile properties of a Zn-containing grain boundary and a clean grain boundary (with no Zn atoms) (Ref. 46). The results revealed that the Zn-doped grain boundary had lower strength and elongation than the clean grain boundary. The presence of Zn reduced the strength of the Fe-Fe interatomic bond and changed the electronic structure of the grain boundary, both of which contributed to a significant decrease in grain boundary cohesion (Ref. 46). Consequently, grain boundaries would be susceptible to intergranular cracks at stress levels much lower than those in the uncoated condition.

The stress-assisted grain boundary diffusion mechanism described here can provide an excellent explanation for the observations made in this study. The EBSD characterization of LME cracking (Figs. 4 and 5) demonstrated that LME occurs predominantly along high-angle random boundaries. Additionally, the results indicated that despite having a high proportion of CSL boundaries, the austenitic microstructure is highly susceptible to LME. The primary reason for this can be attributed to the high grain boundary coefficient of Zn in austenitic structures (i.e., FCC crystal structure), resulting in a high diffusion rate along grain boundaries and the occurrence of LME cracks (Ref. 12). The results also showed that CSL boundaries are highly resistant to LME. Therefore, innovative techniques such as grain boundary engineering (GBE) can be used to increase the fraction of CSL boundaries, thereby reducing the formation of LME cracks in austenitic microstructures (Ref. 30). Furthermore, the increase in LME susceptibility with increasing testing temperature can be explained by factors affecting the kinetics of the grain boundary diffusion process. According to Gordon and An (Ref. 43), LME cracking occurs in two stress-controlled stages: (i) the transfer of embrittler atoms (e.g., Zn atoms) from the absorbed to the dissolved state (at the surface) and (ii) diffusion along grain boundaries. Therefore, the Gordon-An model (Ref. 43) suggests that LME cracking is a temperature- and stress-sensitive phenomenon in which an increase in stress level and temperature facilitate the formation of LME cracks. The model also predicts that there exists a critical stress below which no LME-induced fracture can occur. Critical stress is highly dependent on temperature, and its magnitude decreases with an increase in temperature, which is consistent with the findings of this study. Figure 8 illustrates the variation of the maximum tensile strength of the Zn-coated specimens as a function of temperature. Figure 8 shows that the magnitude of tensile stress decreased with increasing temperature. This indicates that temperature plays a significant role in determining the susceptibility to LME cracking, as increasing temperature significantly decreases the critical stress required to trigger LME cracking. The observation is consistent with the mesoscale plastic deformation analysis presented in Fig. 7, which showed that no plastic deformation occurred during LME-induced cracking at 900°C. Based on this observation, the Zn diffusion rate was high enough at this temperature to trigger crack initiation and propagation, even when the applied tensile stress was low.

Based on the results presented in this section, an excellent correlation was found between the LME-induced failure and the underlying mechanism of the LME. Figure 9 summarizes the main findings of this study regarding the role of LME cracking in the degradation of the tensile properties of austenitic microstructures. The uncoated specimen failed with a fully ductile behavior, with void nucleation and void coalescence, and extensive necking before failure. For the Zn-coated specimen, LME-induced cracking was the primary cause of the failure. The results revealed that the LME cracks propagated rapidly through the grain boundaries at a low applied tensile stress, resulting in a catastrophic brittle failure in the Zn-coated specimen.

Conclusions

This study examines the effects of Zn-induced LME cracking on the tensile properties and failure mechanism of austenitic microstructures during a high-temperature tensile test. The results indicate that austenitic steel is highly susceptible to LME cracking at temperatures between 600° and 900°C. With increasing testing temperatures, the susceptibility to LME cracking increased until the sample at 900°C showed

completely brittle behavior lacking both ductility and fracture toughness. The following are the main conclusions that can be drawn from this study:

1. The LME crack propagation path analysis revealed that LME predominantly occurs along high-angle random grain boundaries. Moreover, a detailed failure analysis demonstrated that the Zn-coated sample failed due to an intergranular fracture mechanism in which no plastic deformation was applied to the grains during deformation.

2. The premature failure of the Zn-coated authentic microstructure was correlated to the mechanism responsible for the formation of LME cracks. Stress-assisted grain boundary diffusion is the most plausible explanation for the failure of the specimen at lower tensile stress when compared to the uncoated specimen.

The results of this study provide further evidence of the high susceptibility of austenitic microstructures to LME cracking. The results also clearly demonstrate the critical role of temperature in LME crack formation, which can be used to gain a deeper understanding of this complex phenomenon during the resistance spot welding process. According to the present study, stress-assisted grain boundary diffusion is the most plausible mechanism responsible for the occurrence of LME cracks. This leads to the conclusion that any factor that impedes the grain boundary diffusion mechanism, such as decreased temperatures, reduced tensile stress, or microstructures with a low grain boundary diffusion rate, can potentially reduce the issue of LME in Zn-coated automotive steels. In the case of austenitic microstructures with a high grain boundary diffusion rate of Zn, novel techniques like grain boundary engineering (GBE) can be employed to enhance the fraction of coincident site lattice (CSL) boundaries and mitigate the issue of LME.

Acknowledgments

The authors would like to thank the Natural Sciences and Engineering Research Council of Canada (NSERC), the Canada Research Chairs (CRC) program, the American Welding Society (AWS), and the International Zinc Association (Durham, N.C.) for their financial support and providing material to carry out this work.

References

1. Midawi, A. R. H., Kistampally, S., and Biro, E. 2021. Effect of coating and welding wire composition on AHSS GMA welds. *Welding Journal* 100(12): 396-s to 409-s. DOI: 10.29391/2021.100.035

2. Murugan, S. P., Vijayan, V., Ji, C., and Park, Y. D. 2020. Four types of LME cracks in RSW of Zn-coated AHSS. *Welding Journal* 99(8): 75-s to 92-s. DOI: 10.29391/2020.99.008

3. Ghatei-Kalashami, A., Kermanpur, A., Najafizadeh, A., and Mazaheri, Y. 2016. Development of a high strength and ductile Nb-bearing dual phase steel by cold-rolling and intercritical annealing of the ferrite-martensite microstructures. *Materials Science and Engineering* 658: 355–366. DOI: 10.1016/j.msea.2016.02.028

4. Ghatei-Kalashami, A., Han, X., Goodwin, F., and Zhou, Y. N. 2020. The influence of modified annealing during the galvanizing process on the resistance spot welding of the CMn1.8Si advanced high strength steel. *Surface and Coatings Technology* 381. DOI: 10.1016/j.surfcoat.2019.125181

5. Ghatei-Kalashami, A., Zhang, S., Shojaee, M., Midawi, A. R. H., Goodwin, F., and Zhou, Y. N. 2022. Failure behavior of resistance spot welded advanced high strength steel: the role of surface condition and initial microstructure. *Journals of Materials Processing Technology* 299: 117370. DOI: 10.1016/j.jmatprotec.2021.117370

6. Marder, A. R. 2000. The metallurgy of zinc-coated steel. *Progress in Materials Science* 45(3): 191–271. DOI: 10.1016/S0079-6425(98)00006-1

7. Lee, C. W., Fan, D. W., Sohn, I. R., Lee, S. J., and De Cooman, B. C. 2012. Liquid-metal-induced embrittlement of Zn-coated hot stamping steel. *Metallurgical and Materials Transactions A* 43(13): 5122–5127. DOI: 10.1007/s11661-012-1316-0

8. Cho, L., Kang, H., Lee, C., and De Cooman, B.C. 2014. Microstructure of liquid metal embrittlement cracks on Zn-coated 22MnB5 press-hardened steel. *Scripta Materialia* 90(1): 25–28. DOI: 10.1016/j.scriptamat.2014.07.008

9. Ghatei-Kalashami, A., DiGiovanni, C., Razmpoosh, M. H., Goodwin, F., and Y. N. Zhou. 2020. The role of internal oxides on the liquid metal embrittlement cracking during resistance spot welding of the dual phase steel. *Metallurgical and Materials Transactions A* 51(5): 2180–2191. DOI: 10.1007/s11661-020-05702-7

10. Böhne, C., Meschut, G., Biegler, M., and Rethmeier, M. 2022. The influence of electrode indentation rate on LME formation during RSW. *Welding Journal* 101(7): 197-s to 207-s. DOI: 10.29391/2022.101.015

11. Tumuluru, M. 2019. Effect of silicon and retained austenite on the liquid metal embrittlement cracking behavior of GEN3 and high-strength automotive steels. *Welding Journal* 98: 351-s to 364-s. DOI: 10.29391/2019.98.029

12. Ghatei-Kalashami, A., Khan, M. S., Goodwin, F., and Zhou, Y. N. 2023. Investigating zinc-assisted liquid metal embrittlement in ferritic and austenitic steels: correlation between crack susceptibility and failure mechanism. *Materials Characterization* 195: 112502. DOI: 10.1016/j.matchar.2022.112502

13. Ghatei-Kalashami, A. 2023. An integrative investigation of liquid metal embrittlement in the Fe-Zn system: From responsible mechanisms to mitigation strategies. University of Waterloo. hdl.handle.net/10012/19228

14. Kim, D., Kang, J., and Kim, S. 2018. Heating rate effect on liquid zn-assisted embrittlement of high Mn austenitic steel. *Surface and Coatings Technology* 347: 157–163. DOI: 10.1016/j.surfcoat.2018.04.081

15. Kang, J., Kim, D., Kim, D. H., and Kim, S. 2019. Fe-Zn reaction and its influence on microcracks during hot tensile deformation of galvanized 22MnB5 steel. *Surface and Coatings Technology* 357: 1069–1075. DOI: 10.1016/j.surfcoat.2018.08.010

16. Ghatei-Kalashami, A., Ghassemali, E., Digiovanni, C., Goodwin, F., and Zhou, N. Y. 2021. Occurrence of liquid-metal-embrittlement in a fully ferritic microstructure. *Materialia* 101036. DOI: 10.1016/j.mtla.2021.101036

17. Ghatei-Kalashami, A., Ghassemali, E., Digiovanni, C., Goodwin, F., and Zhou, N. Y. 2022. Liquid metal embrittlement cracking behavior in iron-zinc (Fe/Zn) couple: Comparison of ferritic and austenitic microstructures. *Materials Letters* 324: 132780. DOI: 10.1016/j.matlet.2022.132780

18. Razmpoosh, M. H., DiGiovanni, C., Zhou, Y. N., and Biro, E. 2021. Pathway to understand liquid metal embrittlement (LME) in Fe-Zn couple: From fundamentals toward application. *Progress Materials in Science* 121: 100798. DOI: 10.1016/j.pmatsci.2021.100798

19. Ghatei-Kalashami, A., Digiovanni, C., Razmpoosh, M. H., Goodwin, F., and Zhou, Y. N. 2020. The effect of silicon content on liquid-metal-embrittlement susceptibility in resistance spot welding of galvanized dual-phase steel. *Journal of Manufacturing Processes* 57: 370–379. DOI:10.1016/j.jmapro.2020.07.008

20. Dong, W., Pan, H., Lei, M., Ding, K., and Gao, Y. 2022. Zn penetration and its coupled interaction with the grain boundary during the resistance spot welding of the QP980 steel. *Scripta Materialia* 218: 114832. DOI: 10.1016/j.scriptamat.2022.114832

21. Dong, W., Ding, K., Pan, H., Lei, M., Wang, L., and Gao, Y. 2022. Role of Si content in the element segregation of galvanized QP980 advanced high strength steel. *JOM* 2–9. DOI:10.1007/s11837-022-05284-2

22. Digiovanni, C., Kalashami, A. G., Goodwin, F., Biro, E., and Zhou, Y. N. 2021. Occurrence of sub-critical heat affected zone liquid metal embrittlement in joining of advanced high strength steel. *Journal of Materials Processing Technology* 288: 116917. DOI: 10.1016/j.jmatprotec.2020.116917

23. ASTM. 2017. A240/A240M-17, *Standard Specification for Chromium and Chromium-Nickel Stainless Steel Plate, Sheet, and Strip for Pressure Vessels and for General Applications*.

24. Ghatei-Kalashami, A., Khan, M. S., Lee, M. Y., and Zhou, Y. N. 2022. High-temperature phase evolution of the ZnAlMg coating and its effect on mitigating liquid-metal-embrittlement cracking. *Acta Materialia* 229: 117836. DOI: 10.1016/j.actamat.2022.117836

25. Mainprice, D., Bachmann, F., Hielscher, R., and Schaeben, H. 2015. Descriptive tools for the analysis of texture projects with large datasets using mtex: strength, symmetry and components. *Geological Society London Special Publications* 409(1): 251–271. DOI: 10.1144/SP409.8

26. Razmpoosh, M. H., Macwan, A., Goodwin, F., Biro, E., and Zhou, Y. 2020. Role of random and coincidence site lattice grain boundaries in liquid metal embrittlement of iron (FCC)-Zn couple. *Metallurgical and Materials Transactions A* 51(8): 3938–3944. DOI: 10.1007/s11661-020-05857-3

27. Kalsar, R., Kumar, L., and Suwas, S. 2018. Grain boundary engineering of medium Mn TWIP steels: A novel method to enhance the mechanical properties. *ISIJ International* 58(7): 1324–1331. DOI: 10.2355/isijinternational.ISIJINT-2017-710

28. Gao, J., Tan, J., Wu, X., and Xia, S. 2019. Effect of grain boundary engineering on corrosion fatigue behavior of 316LN stainless steel in borated and lithiated high-temperature water. *Corrosion Science* 152: 190–201. DOI: 10.1016/j.corsci.2019.01.036

29. Kwon, Y. J., Jung, S. P., Lee, B. J., and Lee, C. S. 2018. Grain boundary engineering approach to improve hydrogen embrittlement resistance in Fe-Mn-C TWIP steel. *International Journal of Hydrogen Energy* 43(21): 10129–10140. DOI: 10.1016/j.ijhydene.2018.04.048

30. Razmpoosh, M. H., Macwan, A., Goodwin, F., Biro, E., and Zhou, Y. 2020. Suppression of liquid-metal-embrittlement by twin-induced grain boundary engineering approach. *Materialia* 11: 100668. DOI: 10.1016/j.mtla.2020.100668

31. Hu, H., Zhao, M., Chen, S., and Rong, L. 2020. Effect of grain boundary character distribution on hydrogen embrittlement in Fe-Ni based alloy. *Materials Science and Engineering A* 780: 139201. DOI: 10.1016/j.msea.2020.139201

32. Ghatei-Kalashami, A., Kermanpur, A., Ghassemali, E., Najafizadeh, A., and Mazaheri, Y. 2016. Correlation of microstructure and strain hardening behavior in the ultrafine-grained Nb-bearing dual phase steels. *Materials Science and Engineering A* 678: 215–226. DOI: 10.1016/j.msea.2016.09.108

33. Murugan, S. P., Jeon, J. B., Ji, C., and Park, Y. 2020. Liquid zinc penetration induced intergranular brittle cracking in resistance spot welding of galvannealed advanced high strength steel. *Welding in the World* 64(11): 1957–1969. DOI: 10.1007/s40194-020-00975-3

34. Rui, S. S., Han, Q. N., Wang, X., Li, S., Ma, X., Su, Y., Cai, Z., Du, D., and Shi, H. J. 2021. Correlations between two EBSD-based metrics kernel average misorientation and image quality on indicating dislocations of near-failure low alloy steels induced by tensile and cyclic deformations. *Materials Today Communications* 27: 102445. DOI: 10.1016/j.mtcomm.2021.102445

35. Rui, S. S., Shang, Y. B., Fan, Y. N., Han, Q. N., Niu, L. S., Shi, H. J., Hashimoto, K., and Komai, N. 2018. EBSD analysis of creep deformation induced grain lattice distortion: A new method for creep damage evaluation of austenitic stainless steels. *Materials Science and Engineering A* 733: 329–337. DOI: 10.1016/j.msea.2018.07.058

36. Nzogang, B. C., Bouquerel, J., Cordier, P., Mussi, A., Girard, J., and Karato, S. 2018. Characterization by scanning precession electron diffraction of an aggregate of bridgmanite and ferropericlase deformed at HP-HT. *Geochemistry, Geophysics, Geosystems* 19(3): 582–594. DOI: 10.1002/2017GC007244

37. Beal, C., Kleber, X., Fabrègue, D., and Bouzekri, M. 2012. Embrittlement of a high manganese TWIP steel in the presence of liquid zinc. *Materials Science Forum* 706–709: 2041–2046. DOI: 10.4028/www.scientific.net/MSF.706-709.2041

38. Beal, C., Kleber, X., and Bouzekri, M. 2012. Liquid zinc embrittlement of twinning-induced plasticity steel. *Scripta Materialia* 66(12): 1030–1033. DOI: 10.1016/j.scriptamat.2011.12.040

39. Beal, C., Kleber, X., Fabregue, D., and Bouzekri, M. 2012. Embrittlement of a zinc coated high manganese TWIP steel. *Materials and Science Engineering A* 543: 76–83. DOI: 10.1016/j.msea.2012.02.049

40. Kang, J., Hong, S., Kim, J., and Kim, S. 2020. Zn-induced liquid metal embrittlement of galvanized high-Mn steel: Strain-rate dependency. *Materials and Science Engineering A* 793: 139996. DOI: 10.1016/j.msea.2020.139996

41. Prasad, S., Kim, J., Kim, J., Wan, Y., Lee, C., Bae, J., and Park, Y. 2020. Role of liquid Zn and α-Fe (Zn) on liquid metal embrittlement of medium Mn steel: An ex-situ microstructural analysis of galvannealed coating during high temperature tensile test. *Surface and Coatings Technology* 398: 126069. DOI: 10.1016/j.surfcoat.2020.126069

42. Kang, H., Cho, L., Lee, C., and De Cooman, B. C. 2016. Zn penetration in liquid metal embrittled TWIP steel. *Metallurgical and Materials Transactions* 47(6): 2885–2905. DOI: 10.1007/s11661-016-3475-x

43. Gordon, P., and An, H. H. The mechanisms of crack initiation and crack propagation in metal-induced embrittlement of metals. *Metallurgical Transactions A* 13: 457–472. DOI: 10.1007/BF02643354

44. DiGiovanni, C., Ghatei-Kalashami, A., Biro, E., and Zhou, Y. N. 2021. Liquid metal embrittlement transport mechanism in the Fe/Zn system: Stress-assisted diffusion. *Materialia* 18: 101153. DOI: 10.1016/j.mtla.2021.101153

45. Ikeda, Y., Yuan, R., Chakraborty, A., Ghassemi-Armaki, H., Zuo, J. M., and Maaß, R. 2022. Early stages of liquid-metal embrittlement in an advanced high-strength steel. *Materials Today Advances* 13: 100196. DOI: 10.1016/j.mtadv.2021.100196

46. Peng, W., Peng, H., Wu, G., and Zhang, J. 2020. Effect of zinc-doping on tensile strength of Σ 5 Bcc Fe symmetric tilt grain boundary. *Computational Materials Science* 171: 109204. DOI: 10.1016/j.commatsci.2019.109204

ALI GHATEI-KALASHAMI (*aghateik@uwaterloo.ca*) and **Y. NORMAN ZHOU** are with the Department of Mechanical and Mechatronics Engineering, University of Waterloo, Waterloo, Ontario, Canada.